

Shaking table tests on a three-arch type subway station structure in a liquefiable soil

Guoxing Chen · Su Chen · Chengzhi Qi · Xiuli Du ·
Zhihua Wang · Weiyun Chen

Received: 12 March 2014 / Accepted: 4 September 2014 / Published online: 19 September 2014
© Springer Science+Business Media Dordrecht 2014

Abstract A series of large-scale shaking table tests were performed to investigate the damage mechanisms of a three-arch type subway station structure in a liquefiable soil experiencing strong motions. Methods to measure the displacement included the vision-based displacement test and the fiber Bragg grating test to measure the strain of the galvanized steel wire. Sand boils, waterspouts, ground surface cracks and settlements, and buoyancy movement of the model structure were observed. When the peak excess pore pressure ratios dramatically increased, the Arias intensity also dramatically increased. The peak acceleration of the model soil also almost coincided with liquefaction of the model soil. The seismic responses of the model structure and the soil were shown to be more sensitive to input motions with larger low-frequency components, the phenomenon of high frequency filtering and low frequency amplification effect of the liquefied soil were observed. The peak tensile strain located at the top and bottom of the center pillars was larger than that obtained at the subarch, while the peak tensile strain at the atrium arch was the smallest. The peak strain at the primary and secondary observation sections were remarkably affected by the spatial effect. The results can provide valuable insight into the seismic investigation of these subway structures.

Keywords Shaking table test · Liquefiable soil · Three-arch type subway station structure · Damage mechanism · Vision-based displacement test method · Fiber Bragg grating test method

G. Chen (✉) · S. Chen · Z. Wang · W. Chen
Institute of Geotechnical Engineering, Nanjing University of Technology, Nanjing 210009, China
e-mail: gxc6307@163.com

G. Chen · S. Chen · Z. Wang · W. Chen
Civil Engineering and Earthquake Disaster Prevention Center of Jiangsu Province, Nanjing 210009, China

C. Qi
College of Civil and Transportation Engineering, Beijing University of Civil Engineering and Architecture,
Beijing 100044, China

X. Du
College of Architecture and Civil Engineering, Beijing University of Technology, Beijing 100022, China

1 Introduction

With rapid development and urbanization in China, exploitation and utilization of underground space has become a major concern in China. Through the end of 2013, subways have been built or construction approved in 37 Chinese cities with a total operating mileage of subways of approximately 2,400 km and approximately 1,600 operating subway stations. Before the 1995 Kobe earthquake in Japan, underground structures were assumed to be earthquake resistant. However, the Kobe earthquake showed that underground structures are also vulnerable to seismic damage, as a large number of central reinforced concrete pillars of the underground subway stations cracked. There are several possible reasons for this damage, such as strong ground motions and permanent ground movements (Samata et al. 1997; Schiff 1998; An et al. 1997). The 1999 Chi-Chi earthquake in Taiwan, China, caused severe damage to underground gas and water pipelines. In addition, during the 2008 Wenchuan earthquake in China, Chengdu city, located in the region of intensity VI according to the national standard Seismic Intensity Scale of China GB/T17742-1999, had underground subway stations with seismic designs for intensity VII that suffered damage. Typical damage, such as segmental cracking, spalling, dislocation and water seepage in the lining, occurred (Ling et al. 2009). Observations of major earthquake events showed that the causes of severe damage to underground structures may be slope instability, soil liquefaction, fault displacement or earthquake wave propagation (Hashash et al. 2001). Hence, it is important to determine the seismic response of soil and the damage mechanism of underground structures during the large earthquakes.

Centrifuge and shaking table test are two important approaches to study seismic damage mechanisms and failure patterns for underground structures. In the last few years, shaking and centrifuge table tests have been performed by many researchers to investigate the seismic performance of underground structures and to check current design and analysis methods. Iwatate et al. (2000) launched shaking table tests to investigate the failure mechanism of subway structures in the 1995 Kobe earthquake. Tamari and Towhata (2003) conducted a series of shaking table tests on a flexible rectangular cross-section structure in liquefiable ground. Ohtomo et al. (2001, 2003) carried out shaking table tests on a large tunnel model (3.0 m × 1.75 m × 0.97 m, scale ratio 1/3–1/4) to investigate the soil–structure–interaction (SSI) based on the assumption of a two-dimensional plane strain model. Chen et al. (2007, 2010a, 2010b, 2013) have conducted a series of large-scale shaking table tests on underground subway structures with various cross sections (including two-story and two-span subway station structures, three-story and three-span subway station structures and a circular tunnel structure) in liquefiable ground. A substantial amount of data including soil and structure acceleration, excess pore pressure, earthquake-induced ground settlement, the strains of the model structure and dynamic soil pressure acting on the model structure were recorded and discussed. Liu et al. (2010), Han (2011), and Ling et al. (2012) conducted a series centrifuge shaking table model tests on one-story and three-span subway stations, a circular tunnel, and one-story and two-span subway stations, respectively. These works could expand our knowledge on seismic performance of different cross section underground structures that are subjected to earthquake attack in liquefiable soil.

However, these studies only focused on the behavior of rectangular underground structures or circular tunnels. Few experimental results or numerical simulations are available in the literature on seismic performance of arch-type underground structures. The following two factors are identified: (1) it is difficult to make arch model structures, especially a structure containing both pillars and arches, (2) practical projects including this type of structure are rare. In view of this, we have designed and conducted a series of shaking table tests on a

scaled three-arch type model subway structure in liquefiable soil. The main purpose of this series of 1-g shaking table model tests is to expand our knowledge of the seismic performance of arch type underground structures.

2 Shaking table test

2.1 Test apparatus and similitude ratio design

The seismic characteristics of a three-arch type underground subway station structure have been studied using the shaking table at Nanjing University of Technology. The dimensions of the shaking table are 3.36 m × 4.86 m in plane. The maximum acceleration of shaking table is 1 g with a maximum proof model mass of 25 tons, where g is the gravitational acceleration. The frequency of the input motion ranges from 0.1 to 50 Hz. The net size of the independently developed laminar shear model box is 3.5 m × 2.0 m × 1.7 m. This laminar shear model box can effectively eliminate the reflection and scattering of the seismic wave at the boundary of the box (Chen et al. 2010c, 2013). The testing data of the model structure and liquefiable model soil were collected in real time by an independently developed dynamic signal acquisition system (Han et al. 2010). This study employed the scaling laws recommended by Maymand (1998). Based on these principles, the similarity relationship among the physical quantities can be deduced from the Buckingham π theorem. Based on the characteristics of the model structure and soil, various basic physical quantities, including the length, elastic modulus, and acceleration of the model structure as well as the shear wave velocity, density, and acceleration of the model soil, are selected. The similarity ratios of the model structure and soil are given in Table 1.

2.2 Preparing the model soil and structure

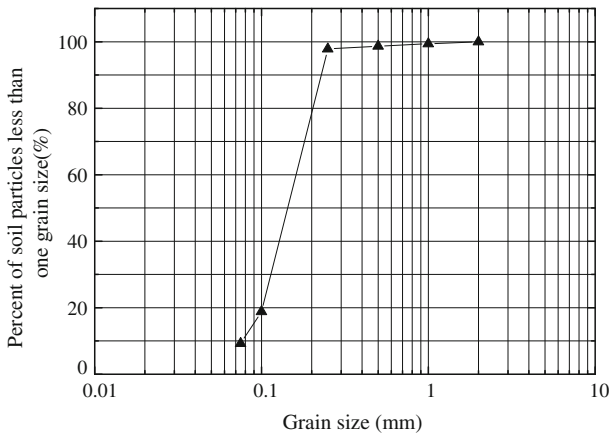
The model soil consists of two layers with a top clay layer 150 mm thick and a bottom saturated fine sand layer 1,250 mm thick. During preparation, the soil was placed in the shear box layer by layer. Each layer was tamped backfill approximately 250 mm thick. The water sedimentation method was used to saturate the model soil. After preparation, the model soil was allowed to stand for 7 days in its natural state in the laboratory. Before the test, the soil characteristics of the clay and fine sand used in the shaking table test were measured by conventional soil tests. The unit weight of the clay is 1,660 kg/m³, water content is 15.6 %,

Table 1 Similitude ratio of the model structure and soil

Types	Physical quantity	Similitude relation	Similitude ratio	
			Model structure	Model soil
Geometry properties	Length l	S_l	1/20	1/4
	Linear displacement r	$S_r = S_l$	1/20	1/4
Material properties	Equivalent density ρ	$S_\rho = S_E/S_l S_a$	5	1
	Elastic modulus E	S_E	1/4	–
Dynamic properties	Mass m	$S_m = S_\rho \cdot S_l^3$	0.2236	–
	Frequency ω	$S_\omega = 1/S_l$	0.2236	2
	Acceleration a	S_a	1	1
	Duration t	$S_t = \sqrt{S_l/S_a}$	0.2236	1/2

Table 2 Material properties of the fine sand

Material	Unit weight (kN/m ³)	Friction angle (°)	Maximum/minimum void ratio	Relative density	Permeability (m/s)	Uniformity coefficient	Coefficient of curvature
Sand	17.8	20.6	1.14/0.62	0.43	1.25×10^{-4}	2.31	1.07

**Fig. 1** Grain composition of the fine sand used in the shaking table test

liquid limit (LL) is 36.84 %, and plastic limit (PL) is 18.75 %. Material properties of the fine sand are given in Table 2. The grain-size distribution of the fine sand is shown in Fig. 1. A DMT seismograph was adopted to measure the shear velocity of the model soil. Before and after the shaking table test, the average shear wave velocity of the model soil was 90.9 and 113.2 m/s, respectively.

Galvanized steel wire and micro-concrete were used to simulate the steel rebar and concrete, respectively. Before the test, the compression test (specimen size of 70.7 mm × 70.7 mm × 70.7 mm) and elasticity modulus test (specimen size of 70.7 mm × 70.7 mm × 210 mm) of the micro-concrete samples were conducted. The compressive yield strength of the micro-concrete was approximately 7.5 MPa, and the elasticity modulus was approximately 7.9 GPa. The tensile yield strength of concrete-like materials is generally equal to approximately 1/10th the compressive yield strength by the code for designing concrete in China (GB50010-2010). Based on the strength test of the micro-concrete, the concrete mix ratio and amount of galvanized steel wire are determined. Mechanical properties of the micro-concrete and galvanized steel wire are shown in Table 3. Plexiglas with 10 mm thick was used to seal the end of the model structure. A typical section is shown in Fig. 3a. Considering the effect of gravitational forces on the prototype structure and the maximum proof mass of the shaking table, rectangle lead blocks (7 cm × 14 cm × 3 cm) with a total additional mass of 236 kg or 40.6 % of the enough artificial mass was uniformly placed on the model structure. Figure 2 illustrates the distribution of the additional artificial mass on the model structure.

2.3 Input motions and loading conditions

The purpose of the series of shaking table tests is to study the seismic behavior of the three-arch type underground subway station structure in a liquefiable soil, therefore, the input

Table 3 Material properties of the micro-concrete and galvanized steel wire

Material	Concrete mix ratio	Compressive yield strength (MPa)	Tensile yield strength (MPa)	Elastic modulus (GPa)
Micro-concrete	Water:cement:lime:coarse sand = 0.5:1:0.58:5	7.5	0.75 (estimated value)	7.9
Galvanized steel wire	–	–	1,190	200

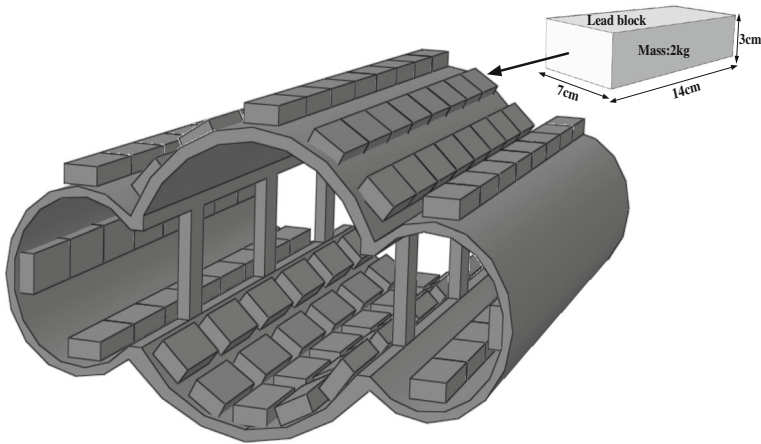


Fig. 2 The distribution of additional weight on the model structure

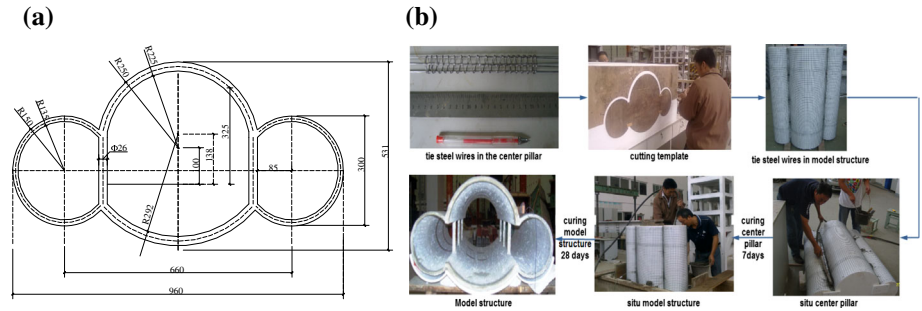


Fig. 3 **a** Typical section and structure reinforcement design and **b** the construction process of the model structure

motions should have different frequency spectrum characteristics and durations. Using the Songpan, Shifang and Taft ground motions as reference waves, the intensity of the input motion was equal to 0.1, 0.3 and 0.5 g, respectively, by adjusting the peak acceleration of the original ground motion. The acceleration time histories and Fourier spectra of the input motions are shown in Fig. 4. The Shifang and Songpan ground motions were recorded at 51SFB and 51SPT seismologic recording stations, respectively, during the Ms8.0 WenChuan earthquake on 12 May 2008 in Sichuan Province, China. The Shifang record original peak acceleration, fault distance and duration were 0.548 g, 10 km and 225 s, respectively, and

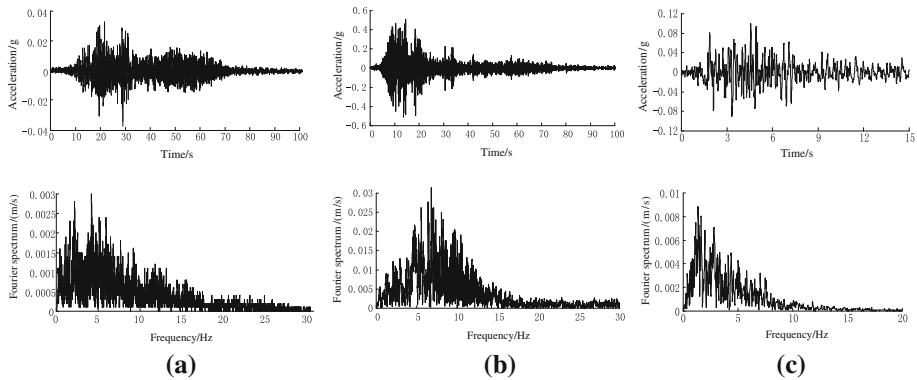


Fig. 4 Ground motion acceleration time histories and Fourier spectra: **a** Shifang record, **b** Songpan record, and **c** Taft record

Table 4 Test cases for the shaking table tests

Test no.	Input motions	Peak acceleration (g)	Duration/s
B1	Flat noise	0.02	180
SP-1	Songpan record	0.1	100
TA-1	Taft record	0.1	15
SF-1	Shifang record	0.1	100
B2	Flat noise	0.02	180
SF-2	Shifang record	0.3	100
SP-2	Songpan record	0.3	100
TA-2	Taft record	0.3	15
B3	Flat noise	0.02	180
SF-3	Shifang record	0.5	100
SP-3	Songpan record	0.5	100
TA-3	Taft record	0.5	15
B4	Flat noise	0.02	180

the Songpan record original peak acceleration, fault distance and duration were 0.041 g, 122 km and 213 s, respectively. The Taft ground motion was recorded at the Taft seismologic recording station during the Ms7.7 Kern County earthquake on 21 July 1952 in California, USA, with an original peak acceleration, fault distance and duration of 0.152 g, 41 km and 54 s, respectively.

The test cases are shown in Table 4. Because dissipation of the excess pore pressure of the model soil was slow, each test was required to stand for at least 1.5–2 h until the excess pore pressure dissipated completely.

2.4 Test instrumentation and layout of sensors

Many sensors were deployed to record various parameters throughout the series of shaking table tests, such as acceleration, excess pore pressure, earthquake-induced ground settlement, structural strain and dynamic soil pressure. The middle cross section of the model box in the shaking direction was selected as the observation section. Sensors are shown in Fig. 5.

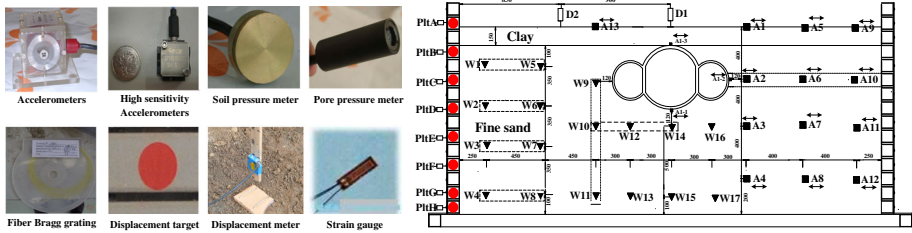


Fig. 5 Sensors used in the shaking table test, and the arrangement plan of the sensors embedded in the observation section (unit: mm)

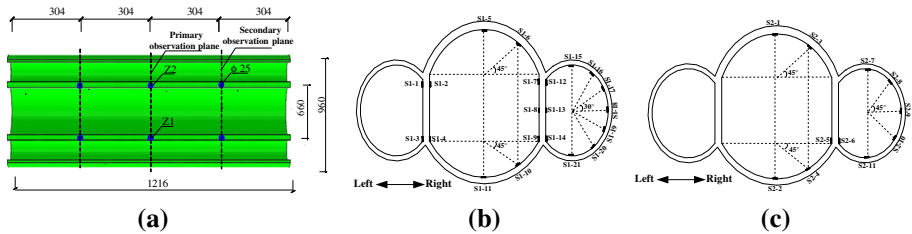


Fig. 6 Layout of the strain sensors in the cross sections of the model structure: **a** observation plane (unit: mm), **b** primary observation section, and **c** secondary observation section

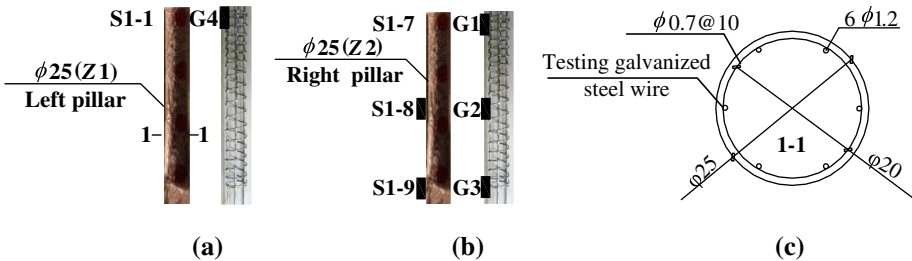


Fig. 7 Distribution map of the FBG and strain gauges in the: **a** left pillar, **b** right pillar, and **c** 1-1 section

The layout of sensors in the model structure are shown in Figs. 6 and 7, which includes 17 accelerometers, 17 pore pressure transducers, 2 displacement transducers, 7 soil pressure transducers, 4 fiber Bragg grating (FBG) strain sensors, 8 dynamic displacement targets and 32 strain gauges, denoted as A, W, D, P, G, Plt and S, respectively. Strain gauges and FBGs were pasted on the model structure surface and galvanized steel wire, respectively, to record the strain data. Based on the calibration for the accelerometers, pore pressure and soil pressure transducers, the measurement accuracy of the sensors was better than 0.5 % F.S., and the resistance value of the strain gauges is $120 \Omega \pm 0.2 \Omega$.

2.5 New measuring technology and its application verification

A vision-based displacement test method was proposed for measuring the horizontal displacement of the model foundation. Moreover, the software was programmed using the method proposed in the kit (Copyright number: 2013SR022133) (Chen and Chen 2013). Bare FBG was adopted to test the strain response of the galvanized steel wire (diameter: 1.2 mm).

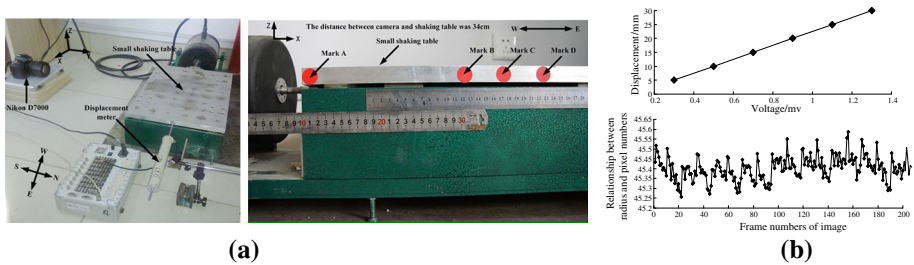


Fig. 8 **a** The verification test system of the vision-based displacement test method and **b** calibration relationship of different sensors

2.5.1 Vision-based displacement test method

The method was based on the basic principle of circle detection using the least squares method (LSM) and video processing technology. First, frames of the dynamic video are captured by a high speed camera, and then preprocessed into continuous static images. These preprocess included image noise reduction, gray scale processing, and adjusting the RGB (red, green, blue) color proportion. Secondly, *Matlab's* image binarization algorithm module for image binarization processing and its image edge detection algorithm for edge detection were used. After the preprocessing, center coordinates and radii of target circles can be obtained by the optimal circle fitting program. Then, the center coordinates are stored successively according to the continuous static image sequence; therefore, the horizontal and vertical displacements of the target circle center in the image space were obtained. By calibrating the relationships between the image pixels and coordinates of the actual objects, the actual displacement can be obtained (Fig. 8).

A small-scale shaking table was used to verify the accuracy and precision of the vision-based dynamic displacement testing method. The validation system is shown in Fig. 9a. Four target circles (radii of all circles were 1 mm) were set for the displacement test, and strain displacement meters were laid on the side of the table board to collect displacement data. Marks A–D represent dynamic displacement testing of the target circles. The testing input excitations were 1, 3, 5 and 8 Hz sine waves. The calibration relationship of the image-object coordinate system is also shown in Fig. 9b with approximately 45.2 pixels representing 1 cm of actual space. The testing precision of the video identification was 0.2 mm.

Under different input excitations, the displacements for the selected mark A were obtained by the strain displacement meter and vision-based displacement test method were compared. The results are shown in Fig. 9. It is clear that the displacement amplitudes and curve shapes obtained by the vision-based dynamic displacement testing method are similar to the shapes obtained by the strain displacement meters. We used a correlation coefficient as a standard for the similarity degree of the curves obtained by the two methods (Hyndmana and Koehlerb 2006). When input sine waves are 1, 3, 5 and 8 Hz, the corresponding correlation coefficients of the displacement curves measured by the two testing methods are 0.994, 0.996, 0.990 and 0.987, respectively.

2.5.2 Laying, packaging and testing processes of the fiber Bragg grating

The working principle of the FBG can be found elsewhere (Hyndmana and Koehlerb 2006). The encapsulation of optical FBG is shown in Fig. 10a. We used alcohol to remove impurities

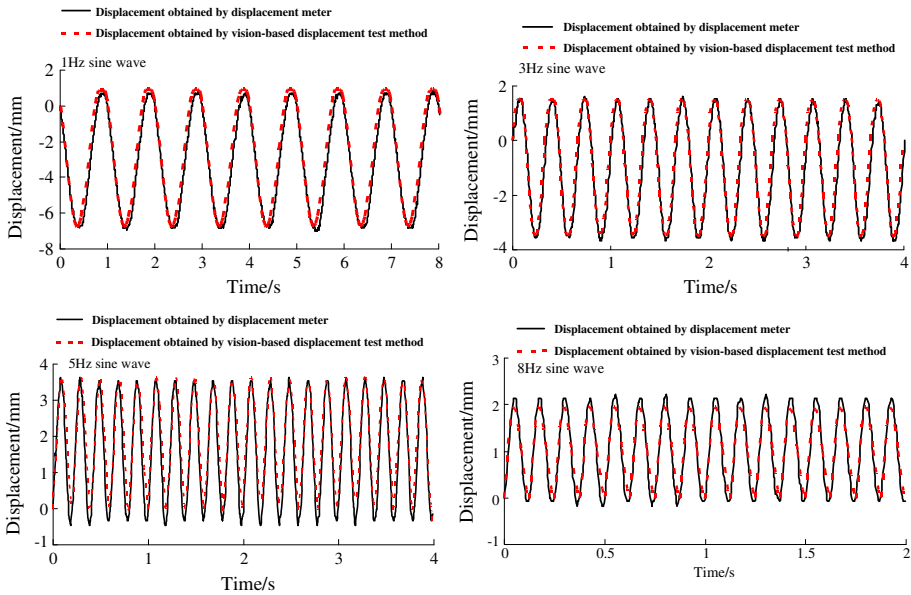


Fig. 9 The comparison between displacements obtained by the strain displacement meter and camera for different input waves

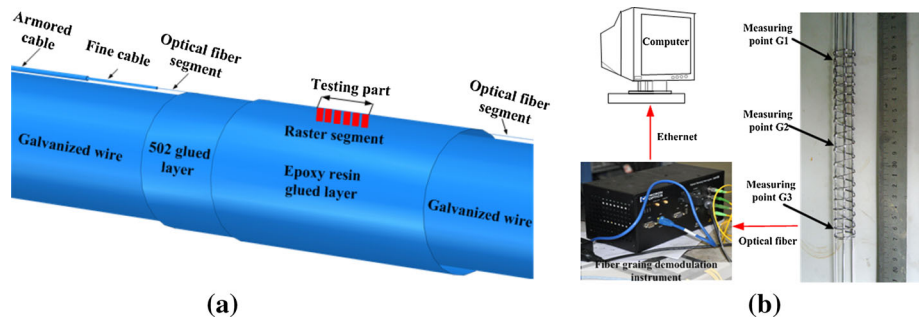
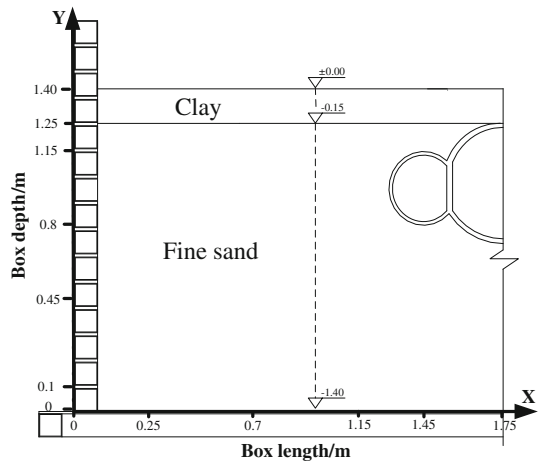


Fig. 10 Packaging and testing processes of the fiber Bragg grating: **a** encapsulation diagram of the optical fiber Bragg grating and **b** the strain test flow chart using the optical fiber Bragg grating

at the test points before gluing; then we used 502 glue (rapid set glue) to paste the raster segment on the test points after alcohol volatilization. After the glue set, we used epoxy resin to encapsulate the optical fiber segment already attached to the galvanized steel wire at the strain measuring points. The same method was used to paste the optical fiber segment on both sides of the galvanized steel wire to prevent the optical fiber segment pulling off the surface of the galvanized steel wire. After the glue hardened, the fiber wire was set into the fine cable and the armored cable was used as the secondary protection of the FBG, which would pass through the micro-concrete segment when casting the micro-concrete.

The FBG strain testing process is shown in Fig. 10b. Signals of the FBG caused by shaking transmit to a dynamic fiber grating demodulation instrument (MOI SM130), which transforms the fiber wavelength signals into strain signals. The demodulated data will be transmitted to a computer by an Ethernet cable.

Fig. 11 The definition of the coordinate system and elevation



2.6 Convention of data processing and coordinate system

Additional signal processing methods were applied to each record of acceleration and strain measured by the tests. First, a baseline correction was made by subtracting the mean of the records. Secondly, the measurement noise of each record at both low and high frequencies was filtered using a Butterworth filter (Bandpass configuration: $F_{\text{pass}} = 0.1$ Hz, $F_{\text{stop}} = 50$ Hz). The time-frequency transformation of the records was performed using the FFT method. Time histories of the excess pore pressure and dynamic soil pressure were decompounded using the five-point moving average method. This method can remove the burr on the excess pore pressure records. The coordinate system convention in this study is depicted in Fig. 11, which illustrates that the left bottom of the box was defined as the original coordinates, and the top of the model soil was defined as the zero level.

3 Macroscopic phenomena of soil and structure

Figure 12a shows the ground surface observed before the test and Fig. 12b, c show the macroscopic phenomena after the test. Soil liquefaction, water accumulation on the ground surface, sand boils and waterspouts were observed in Fig. 12d. Some air bubbles in the region of the sand boils and waterspouts are believed to be caused by the residual air within the model soil, which upwelled with the sand boils and waterspouts. Ground surface settlement and cracks were observed in Fig. 12e. The model structure had an upward movement relative to the model soil. The tiny cracks on the model structure in the bottom of the pillars could be distinguished in Fig. 12f after the test cases with $\text{PGA} = 0.5$ g.

4 Results and interpretation

4.1 Excess pore pressure

4.1.1 Typical pattern of excess pore pressure

The Wildlife Liquefaction Array triggered four times during the Superstition Hills earthquake sequence on 23–24 November 1987, including a Ms 6.2 foreshock approximately

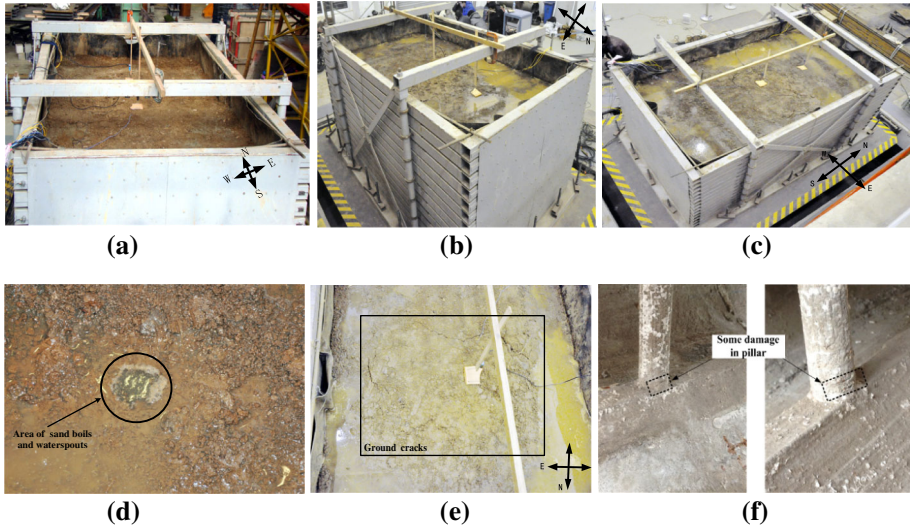


Fig. 12 Macroscopic phenomena of the model soil and structure after test cases with $PGA = 0.5 g$: **a** the ground surface before the test, **b** the ground surface after test observed from the north, **c** the ground surface after the test observed from the south, **d** sand boils and waterspouts, **e** ground surface cracks, and **f** macroscopic phenomena of the model structure after the test

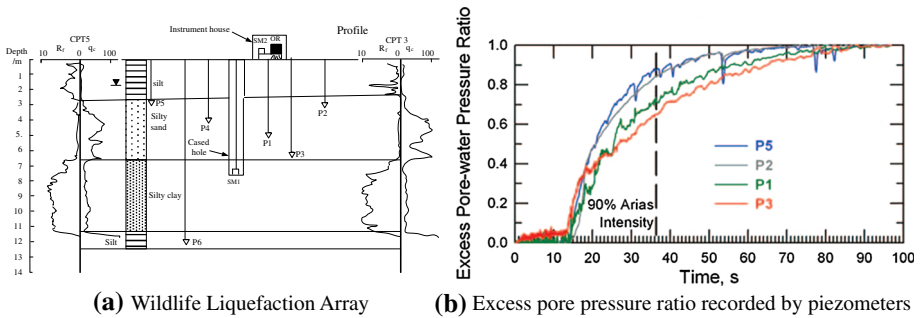


Fig. 13 Sensor layout at the Wildlife Liquefaction Array and excess pore pressure measurements from the Superstition Hills earthquake: **a** schematic cross section of the Wildlife Liquefaction Array (Bennett et al. 1984) and **b** excess pore pressure measurements from the Superstition Hills earthquake

9h before the mainshock. Only the M_s 6.6 mainshock of the Superstition Hills earthquake triggered liquefaction of a 4.3-m-thick sand layer (Holzer and Youd 2007). The excess pore pressure and acceleration time histories were recorded by the US Geological Survey (USGS). Figure 13 shows the layout of the sensors at the Wildlife Liquefaction Array and excess pore pressure ratios recorded during the Superstition Hills earthquake.

There are two standards for the definition of liquefaction in current research. The first uses the standard of 2–2.5 % single amplitude or 5 % double amplitude shear strain as the threshold when liquefaction occurs (Kammerer et al. 2001); the second standard is liquefaction occurs when the excess pore pressure ratio reaches 100 % (Seed and Lee 1966). In cyclic triaxial tests, the single or double amplitude shear strain standard is undoubtedly more appropriate. However, in the shaking table test, there are two difficult problems. The

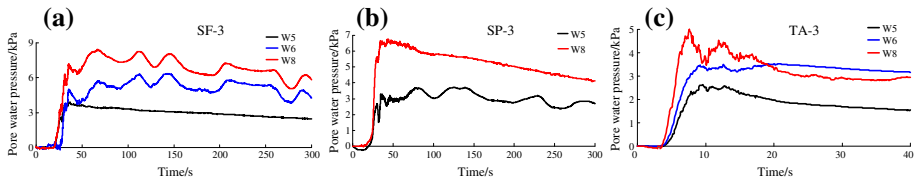


Fig. 14 The development of the excess pore pressure ratio of the model soil for different input motions with PGA = 0.5 g: **a** Shifang ground motion, **b** Songpan ground motion, and **c** Taft ground motion

first problem is that the shear strain of the soil cannot be measured directly during the shaking table test but is calculated by the horizontal measurements of the accelerometers inside the soil (Koga and Matsuo 1990). The second problem is that the threshold value of the low and/or high frequencies with the band-pass filter has a significant effect on the horizontal displacements obtained by the double integration algorithm of the acceleration records, so the stress-strain hysteresis loop of the soil and accuracy of the shear strain of the soil is closely related to the threshold value of the low and/or high frequencies of the band-pass filter (Chen et al. 2012). Hence, the excess pore pressure ratio of $r_u = 100\%$ as the threshold standard for liquefaction was adopted in this paper, where $r_u = EPP/\sigma'_v$, and where EPP is excess pore pressure of soil and σ'_v is the initial effective vertical stress of the soil.

Piezometers W5, W6 and W8, which were buried from the top to the bottom of the model soil in this test, were selected to contrast the development pattern of excess pore pressure with the piezometers P5, P2 and P3, which recorded the Wildlife Liquefaction Array. To show significant liquefaction characteristics, the excess pore pressure of the model soil recorded by piezometers W5, W6 and W8 that experienced input motions with PGA = 0.5 g were shown in Fig. 14. From Figs. 13 and 14, it is clear that the buildup of excess pore pressure measured from the Wildlife Liquefaction Array and shaking table test proceeded mainly through two increasing stages. During the initial stage, excess pore pressure increased slowly and the model soil shows elastic characteristics. During the second stage, excess pore pressure increased rapidly due to the cumulative seismic effect, so the soil particles were forced to roll or slide with respect to adjacent particles and the volume of the soil decreased. However, water was regarded as incompressible. Because the duration of the input motion was fairly short, the model soil was considered to be in an undrained condition during the shaking. These internal contradictions were solved by increasing the excess pore pressure and reducing the effective stress, which is why the development of the excess pore pressure occurred instantly. The main characteristic of the third stage is the excess pore pressure dissipated slowly.

4.1.2 Liquefaction assessment by Arias intensity

The Arias intensity, I_A , is most commonly defined as (Arias 1970):

$$I_A = \frac{\pi}{2g} \int_0^{T_d} a(t)^2 dt \quad (1)$$

where g is the gravitational acceleration; $a(t)$ is the recorded acceleration time-history; and T_d is the duration of the ground motion.

The Arias intensity for the model soil was shown in Fig. 15. It shows that the Arias intensity of the model soil induced by the Shifang motion with a PGA = 0.1 g was

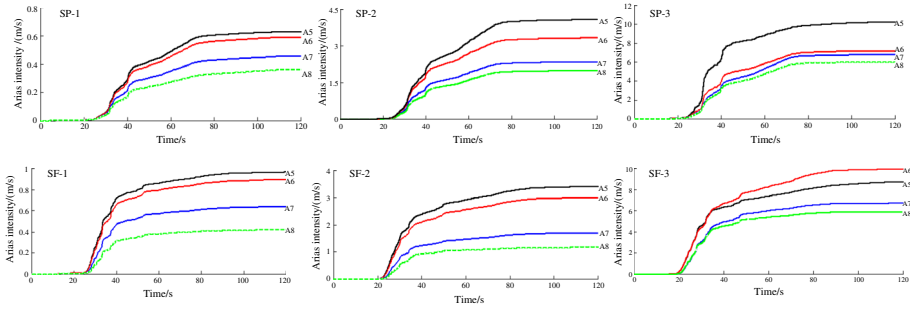


Fig. 15 Time histories of the Arias intensity at different points for the model soil

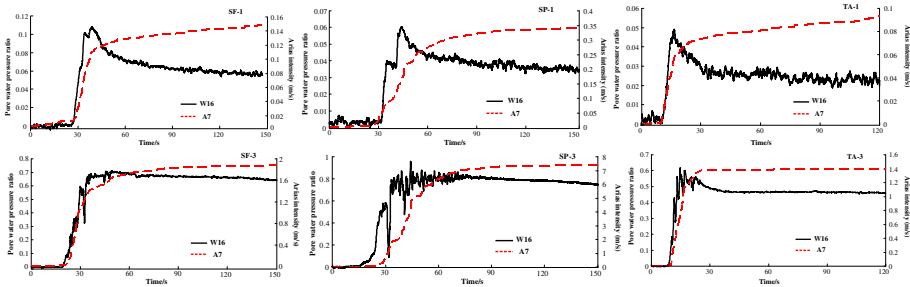


Fig. 16 Time histories of the excess pore pressure ratio and Arias intensity for the model soil

greater than that induced by the Songpan motion. However, the input motions with a higher PGA (e.g., 0.3 and 0.5 g), the Arias intensity of the model soil induced by the Songpan motion was larger than that induced by the Shifang motion. This illustrates that the stiffness of the model soil under strong motions decreased, and the seismic response of the model soil was more sensitive to input motions with larger low frequency components.

The relationship between the Arias intensity at point A7 and excess pore pressure ratios at point W16 under different input motions was illustrated in Fig. 16. Note that when the peak excess pore pressure ratios dramatically increased was when the Arias intensity dramatically increased. For input motions with a PGA = 0.5 g, the Arias intensity at the end of shaking was $I_A = 7.42, 1.89$ and 1.41 m/s for Songpan, Shifang and Taft ground motions, respectively. Accordingly, the peak excess pore pressure ratio at point W16 under input motions with a PGA = 0.5 g was the maximum induced by the Songpan ground motion, the middle induced by the Shifang ground motion, and the minimum induced by the Taft ground motion. In addition, because the shallow soil underwent lower confining pressure and consequently experienced more significant stiffness degradation, the accumulation of the total energy in the upper layer of the model soil was greater than that in the bottom layer of the model soil.

4.1.3 Distribution characteristics of excess pore pressure

Figure 17 shows the distribution of the excess pore pressure ratio of the model soil for different test cases. Software *Surfer* (version 8.0) was adopted to predict the excess pore pressure ratio distribution of the model soil. A lighter shade in Fig. 17 represents higher soil

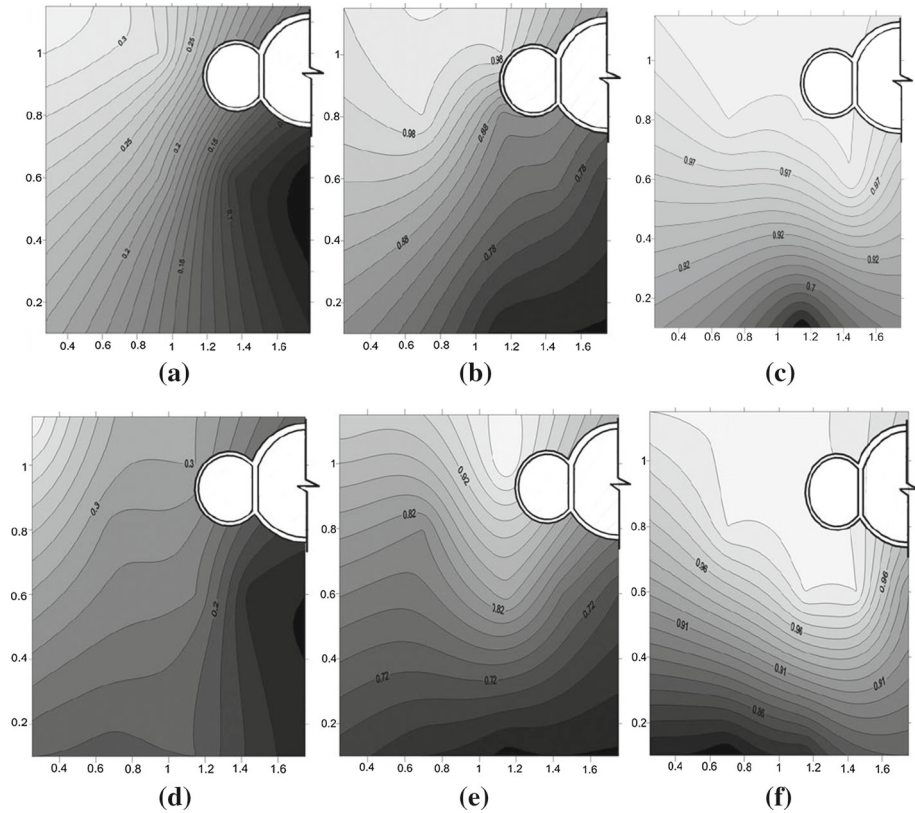


Fig. 17 Contour plot of the peak excess pore pressure ratio for different test cases. The *horizontal* and *vertical coordinate values* are denoted as the length and height, respectively, of the Laminar shear model box (coordinate unit: m). **a** Songpan record with PGA = 0.1 g. **b** Songpan record with PGA = 0.3 g. **c** Songpan record with PGA = 0.5 g. **d** Shifang record with PGA = 0.1 g. **e** Shifang record with PGA = 0.3 g. **f** Shifang record with PGA = 0.5 g

liquefaction potential. From Fig. 17, it is quite clear that the presence of the model structure had a strong effect on the distribution of the excess pore pressure ratio. The excess pore pressure ratio of shallower soil layer was greater than the deeper soil layer, which showed that the liquefaction potential of the shallower soil was higher. Moreover, for input motions with a PGA = 0.1 g, the peak excess pore pressure ratio of the model soil was much less than 1, which means that the model soil was not liquefied during shaking. The shade beneath the model structure was the darkest, which illustrates the soil liquefaction potential at this region was the lowest. This may occur because the ability of soil particles to roll or slide up on adjacent particles was weak under the input motions with lower PGA (e.g., 0.1 g), which results in lower excess pore pressure. The main factor influencing the excess pore pressure distribution was the prophase consolidation pressure of the model soil, which is the region beneath the structure that underwent higher confining pressure during consolidation. However, under input motions with higher PGA (e.g., 0.3 and 0.5 g), the shade in the bottom region of ground was the darkest.

In addition to, it can be seen in Figs. 16 and 17 that as the Arias intensity of the model soil increased, the liquefaction potential of the soil increased.

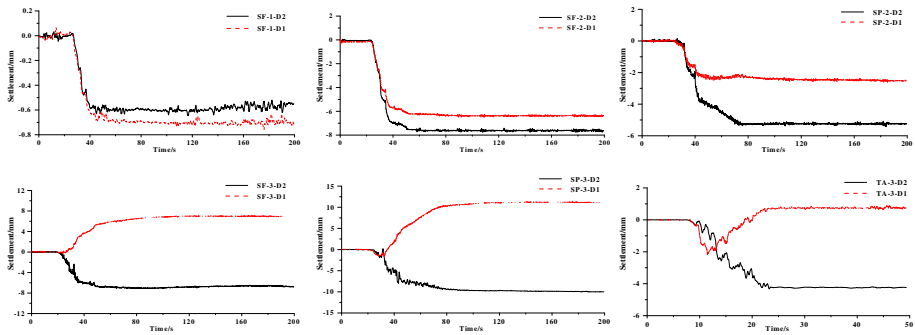


Fig. 18 Time histories of earthquake-induced ground surface settlement from different input motions (unit: mm)

4.2 Earthquake-induced ground settlement

4.2.1 Ground surface settlements

The earthquake-induced ground settlement time-histories are shown in Fig. 18. Larger ground settlement occurred under input motions with greater PGA and longer durations, while ground surface settlements were generally small when the input motions with PGA = 0.1 g (all less than 1 mm). The test records of the earthquake-induced settlement at the ground surface point D1 (above the model structure) and the ground surface point D2 (side above the model structure) were approximately the same for PGA = 0.1 g. However, when the input motions were increased to PGA = 0.3 g, the earthquake-induced settlement at point D1 was significantly smaller than at point D2. During test cases with PGA = 0.5 g, the soil was significantly pushed up at point D1 when larger earthquake-induced settlement occurred at point D2; the final ground surface uplift at point D1 was 11.04, 7.14 and 0.89 mm for the Songpan, Shifang and Taft ground motions, respectively. The uplift of the model structure was caused by two basic factors. First, the model structure is a hollow-type structure, therefore, the structure mass per unit volume is less than the surrounding soil. If the soil liquefied, the buoyancy of the model soil surrounding the structure would increase. Second, the stiffness of the soil after liquefaction would sharply decrease, which would significantly increase the deformation and settlement of the soil. There are differences between the vertical inertial force of the model structure and soil, so relative movement between the model structure and soil would occur. For the test cases with PGA = 0.1 and 0.3 g, the increase in excess pore pressure was not enough to uplift the structure, but in the test case with PGA = 0.5 g, the shallower soil near the structure totally liquefied, while the region beneath the model structure was not fully liquefied. This phenomenon can be explained using the shape of the contour plot of the peak excess pore pressure ratio in Fig. 17.

4.2.2 Mechanism of earthquake-induced ground settlement

Earthquake-induced settlement of the model soil was induced by two physical processes. First, the model soil became dense under the input motion. Secondly, equilibrium of the vertical forces acting on the model structure was lost, which caused a buoyant rise of the model structure.

Table 5 Peak dynamic soil pressure of the subway station structure for different input motions (unit: kPa)

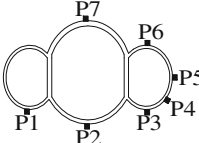
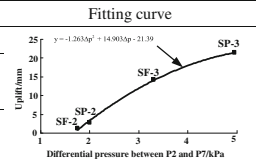
Layout of soil pressure transducers	Loading condition						
	SF-1	SF-2	SF-3	SP-1	SP-2	SP-3	
	P2	0.69	2.36	3.89	0.46	2.36	5.84
	P3	0.24	0.68	2.65	0.17	1.02	3.37
	P4	0.20	1.01	1.68	0.12	0.64	0.99
	P5	0.35	2.45	2.49	0.19	1.47	1.96
	P6	0.18	0.11	0.18	0.15	0.26	0.84
	P7	0.07	0.61	0.59	0.13	0.33	0.89

Table 6 The relationship between the differential soil pressure and uplift of the model structure

Measurement	Loading condition					
	SF-1	SF-2	SF-3	SP-1	SP-2	SP-3
Uplift of the model structure (mm)	0.11	1.26	14.3	0.03	2.81	21.4
Differential soil pressure between points P2 and P7 (kPa)	0.62	1.75	3.3	0.33	2.0	4.95



The first physical process can be verified by the shear wave velocity of the model soil before and after the test. The second physical process was intuitively reflected in the dynamic soil pressure measured on the model structure. The peak of the dynamic soil pressure from different input motions is shown in Table 5. The dynamic soil pressure at point P2 was significantly greater than at point P7, therefore the differential pressure between the points P2 and P7 can be considered to be a force that results from the development of excess pore pressure beneath the model structure. This force caused the buoyant rise of the model structure in the liquefied soil. Table 6 shows the relationship between the differential soil pressure and amount of uplift of the model structure. It was clear that as the PGA of the input motions increases, the differential soil pressure between points P2 and P7 increases. Moreover, the smaller the differential soil pressure between points P2 and P7, the smaller the uplift of the model structure. For the Songpan ground motion with a PGA = 0.5 g, the value of differential pressure between P2 and P7 reaches a maximum at the same time the uplift of model structure also reaches a maximum.

4.3 Lateral displacement of the model foundation

Existing research shows that the laminar shear soil container ensured a more uniform distribution of the shear stress within the soil with minimal boundary effects while allowing relative slip between the laminates. In other words, the soil in the laminar box can move freely in horizontal direction (Chen et al. 2010c). Therefore, the lateral displacement of each aluminum ring (laminar) of the box was approximately identical to the soil displacement within the laminar. Dynamic displacement targets were mounted on the 8 rings of the laminar box, labeled L2, L4, L6, L8, L10, L12, L14 and L15 in Fig. 19. The horizontal and vertical displacements of measuring point PltA on the top of box (L2) are shown in Fig. 20. It is quite clear from these figures that the vertical displacement of L2 was small; the maximum vertical displacements measured by the vision-based displacement test method were all less than 0.6 mm. This shows that the box only moved in horizontal direction under different input

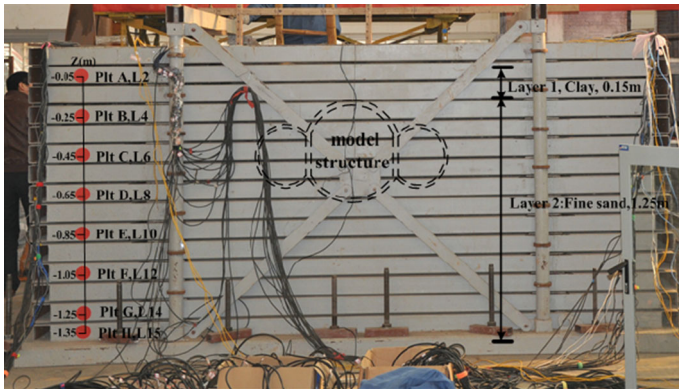


Fig. 19 Layout of the displacement test target sensors (unit: m)

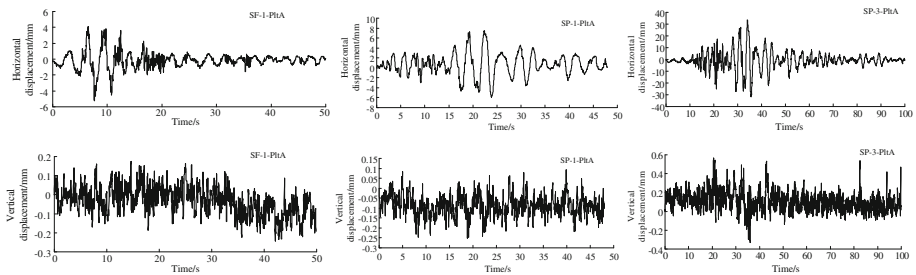


Fig. 20 Horizontal and vertical displacement responses of measuring point PtA from different input motions (unit: mm)

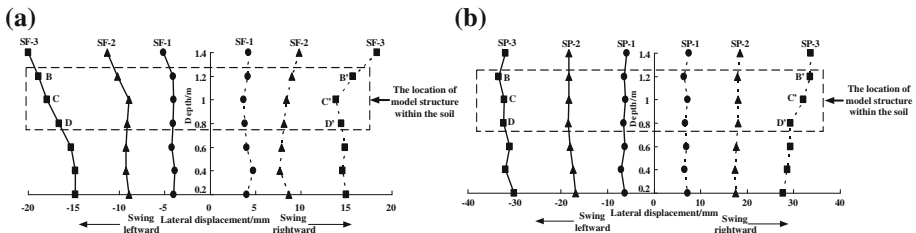


Fig. 21 The maximum lateral displacements of the soil in the test cases: **a** under the Shifang ground motion and **b** under the Songpan ground motion

motions. This conclusion was also verified by the guiding device of the laminar box (sliding rails-ball bearing units system) was smooth enough and did not allow the box to slide in the vertical direction under input motions.

The maximum lateral soil displacements of measuring points (PtA–PtG) were presented in Fig. 21. The maximum lateral displacement data of the soil at different measuring points shows that the soil swinging leftward shows a different degree of asymmetry compared to the soil swinging rightward due to the asymmetry of the input motions between the positive and negative peak displacement. In addition, the effects of several parameters on the soil lateral displacement were addressed. First, as the PGA of input motions increased, the soil lateral displacement also increased. Secondly, the dominant frequency of the input motions had an

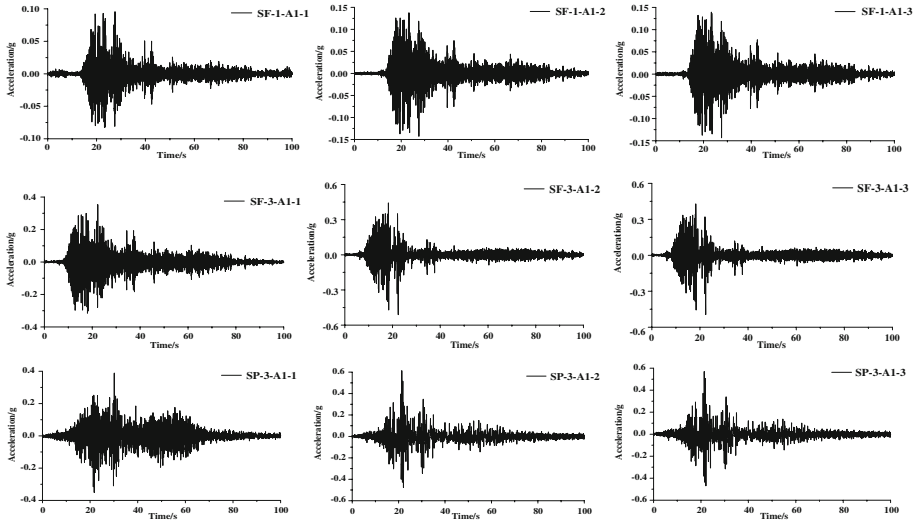


Fig. 22 Acceleration time-histories of the model structure under different input motions

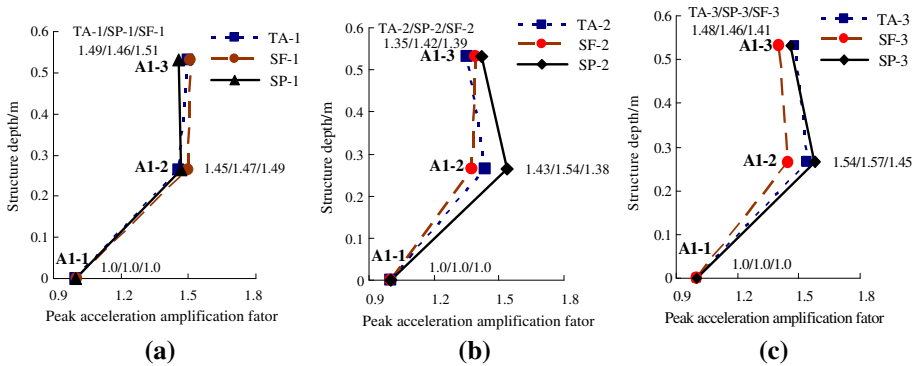


Fig. 23 Peak acceleration amplification factors of the model structure for different input motions. **a** Ground motion with PGA = 0.1 g. **b** Ground motion with PGA = 0.3 g. **c** Ground motion with PGA = 0.5 g

inverse effect on the soil lateral deformation. The maximum lateral displacement of the soil induced by the Songpan ground motion (dominant frequency: 2.09 Hz) was greater than the displacement by the Shifang ground motion (dominant frequency: 6.8 Hz). Furthermore, the maximum lateral displacement of the upper soil (measured at point PltB) was greater than the lower soil (measured at point PltD).

4.4 Acceleration response of the soil–structure system

4.4.1 Acceleration response of the model structure

Figures 22 and 23 show the acceleration time histories and peak acceleration amplification factors of the model structure under different input motions, respectively. The results show that the frequency spectrum characteristics of the input motions do not significantly affect the seismic response of the model structure for input motions with a PGA = 0.1 g. However,

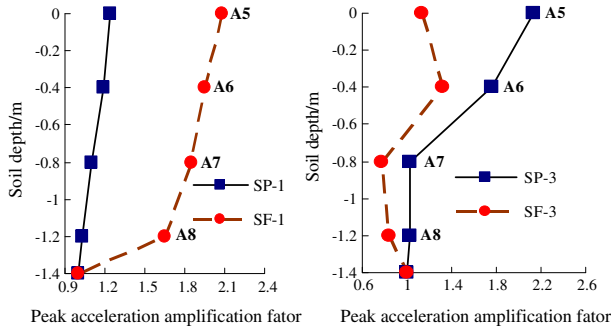


Fig. 24 The peak acceleration amplification factors with soil depth for different input motions

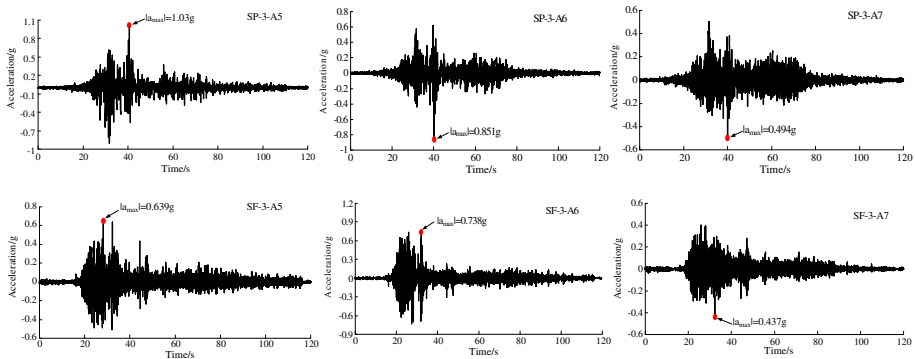


Fig. 25 Accelerograms of the model soil under different input motions at PGA = 0.5 g

for input motions with a higher PGA (e.g., PGA = 0.3 or 0.5 g), the peak acceleration amplification factors induced by the Songpan and Taft ground motions were greater than that induced by the Shifang ground motion. The model structure may be damaged under strong motions and the stiffness of the model structure may decrease. The seismic response of the model structure is more sensitive to strong motions with larger low frequency components for the same PGA.

4.4.2 Acceleration response of the model soil

The peak acceleration amplification factors of the model soil were shown in Fig. 24. For test cases with PGA = 0.1 g, the soil amplification effect induced by the Shifang ground motion (dominant frequency: 6.8 Hz) is greater than that induced by the Songpan ground motion (dominant frequency: 2.09 Hz). The peak acceleration amplification factors increased from the bottom to the top of the model soil, which illustrates the elastic characteristics of the model soil. However, the opposite phenomenon was observed for the test cases with PGA = 0.5 g, which means the input motions with a lower dominant frequency and higher PGA had an inverse effect on soil amplification effect.

The time histories of acceleration for test cases with PGA = 0.5 g are shown in Fig. 25. Close agreement was found between the development of excess pore pressure and acceleration records at shallower fine sand layers, as shown in Fig. 26. For the Songpan and Shifang ground motions with PGA = 0.5 g, it shows the peak acceleration moment of the model soil almost

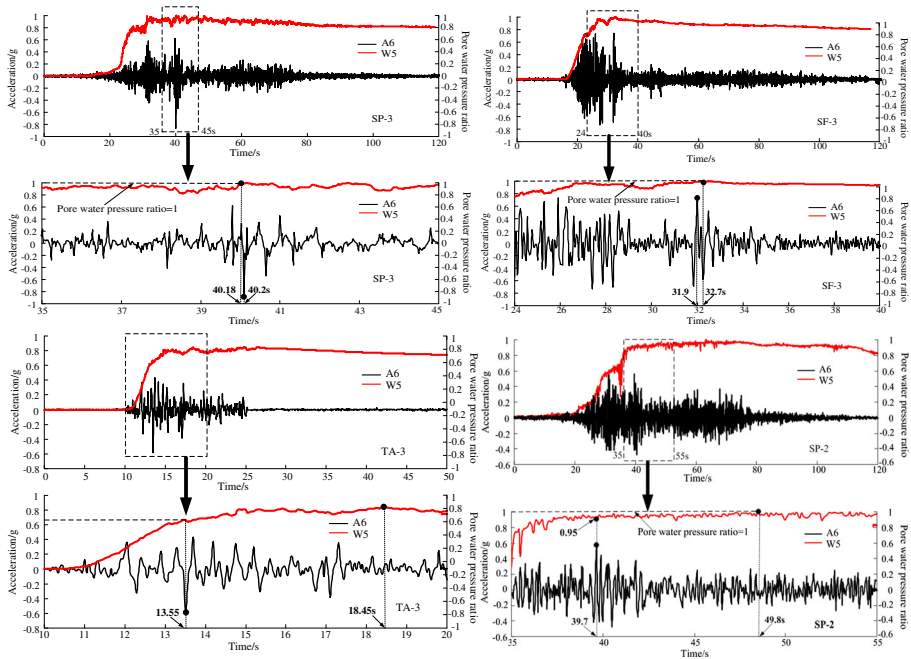


Fig. 26 The relationships between the time histories of acceleration and excess pore pressure of the model soil

coincided with the moment the excess pore pressure ratio of the model soil approximately equaled 1; the moments of soil liquefaction were 40.2 and 32.7 s for the Songpan and Shifang ground motions, respectively. For the Songpan ground motion with $PGA = 0.3\text{ g}$, the peak acceleration of the model soil occurred at 39.7 s when the excess pore pressure ratio reached 0.95. However, for the Taft ground motion with $PGA = 0.5\text{ g}$, the peak acceleration occurred when the pore pressure ratio reached only 0.63. Hence, it is impossible to evaluate the moment that triggers liquefaction at that site (Yasuda et al. 2012).

Figure 27 shows the dynamic amplification factor β of the acceleration response spectra with a damping ratio of 0.05 for the acceleration recorded by accelerometers A5, A6, A7 and A8 under different input motions. Note that the acceleration response spectra β spectra (points A5 and A6) had a significant amplification effect on the short-period components for test cases with $PGA = 0.1\text{ g}$; the amplification effect is especially striking for periods from 0.06 to 0.16 s for the Shifang and Songpan ground motions. As the PGA of input motions increased, the amplification effect of the ground surface acceleration β spectra had obvious selectivity for different frequency components of the input motions and the high frequency filtering phenomenon of the model soil appears. For test cases with $PGA = 0.3\text{ g}$, the dynamic amplification factor β spectra had the multi-peak phenomenon. The multi-peak predominant periods were 0.08, 0.12 and 0.22 s for the Shifang ground motion and 0.16, 0.24 and 0.44 s for the Songpan ground motion, which indicated that the high frequency component of the input motions would be filtered significantly because the soil softened and liquefied. For test cases with $PGA = 0.5\text{ g}$, the phenomena of softened soil and high frequency filtering of the input motions were more obvious. From Fig. 27e, g, it is clear that the short-period of the acceleration response spectra β spectra (points A5 and A6) has been filtered significantly, and the peak of the β spectra certainly moved toward longer periods, which means the spectra

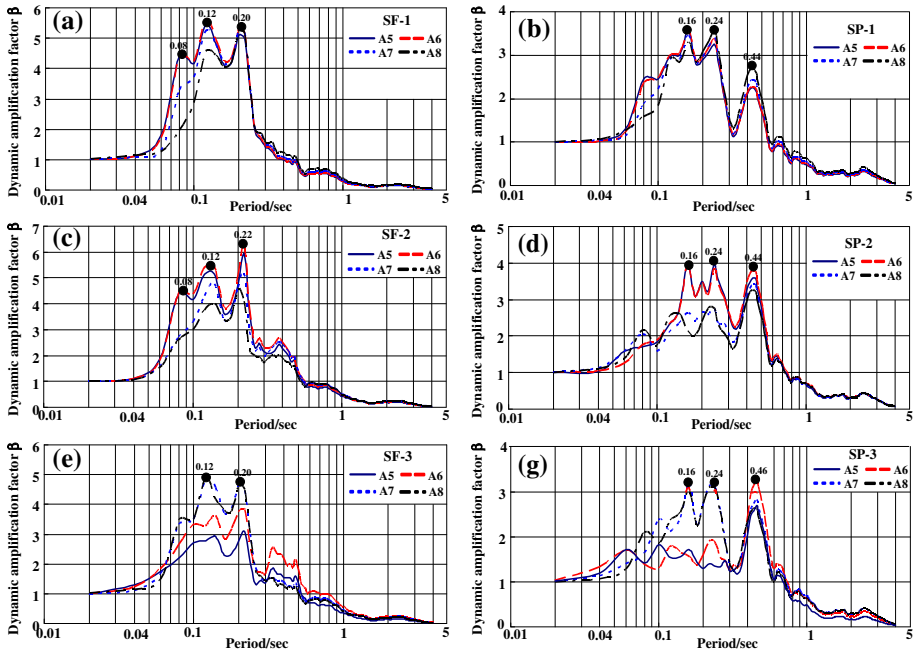


Fig. 27 Acceleration response spectra of the model soil for the observation section for different input motions

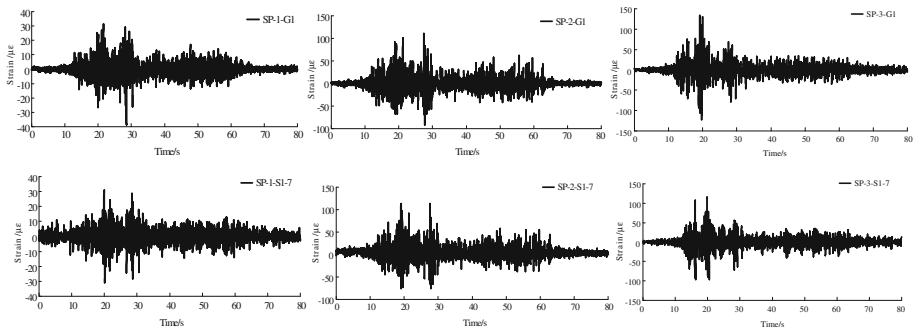


Fig. 28 Time histories of the strain in the galvanized steel wires and micro-concrete on the center pillar under different input motions (unit: $\mu\epsilon$)

of the liquefied soil exhibited concentration and amplification effects for the low frequency components.

4.5 Mechanism of the model structure deformation

4.5.1 Comparison of the strain tested by the strain gauge and fiber Bragg grating

The time-histories of the galvanized steel wire and micro-concrete strain are shown in Fig. 28. It is clear from this figure that the strain response of the galvanized steel wire coincided with the micro-concrete at the top and bottom of the center pillar where the strains were greater than that in other places of the pillar. The strain responses of the galvanized steel wire (point

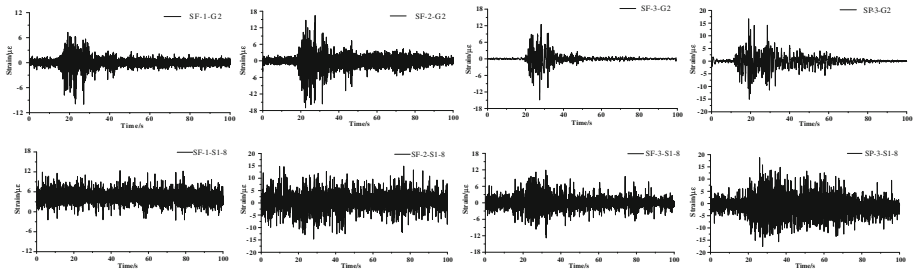


Fig. 29 Time histories of the strain in the galvanized steel wires and micro-concrete on the pillar for different ground motions (unit: $\mu\epsilon$)

G2) and micro-concrete (point S1–8) at the same location are shown in Fig. 29. The strain data obtained by the fiber Bragg grating were obviously better than the data by the strain gauge for the middle part of the center pillar. The fiber Bragg grating test technique is more appropriate when there is large electromagnetic interference, areas with a relatively weak signal, or small-sized base materials.

4.5.2 Strain response of the subway station structure

Figure 30 shows the peak tensile strain distribution of the model structure. It illustrates that the maximum value of the peak tension strain is located at the joints between the pillars and arches. This is because the lateral stiffness of the central pillars is small, the arch–pillar joints experienced higher shear forces and the bending moment for the input motions. In addition, the peak strain at the central part of the right pillar (point S1–8) was small; the peak strain of the center pillar was larger than the subarch; and the peak strain of the atrium arch was the smallest. In addition, because the asymmetry of the input motions and differential settlement of the model soil, the left and right sides of the pillars at the same height had an asymmetric distribution of peak strain. Unfortunately, the strain gauges installed on the inverted arch, labeled S1–10, S1–11, S2–2 and S2–4, did not work during the test. For the atrium arch, the peak strain at the location that intersects a 45° angle with respect to the vertical axis (point S1–6) was larger than the vault of the atrium (point S1–5). In the subarch, the maximum value of the peak tension strain located at both the upper and lower arch walls with intersection angles of 30° – 60° with respect to the vertical axis. The peak tensile strain in this area was significantly larger than in other areas of the subarch. This phenomenon is quite different from the underground circular tunnel structure whose maximum strain occurs at the section $\pm 45^\circ$ from the vertical axis (Kattis et al. 2003; Sedarat et al. 2009).

The vibration of the three-arch type subway station structure was analyzed by *ABAQUS*. There are two requirements that need to be satisfied in the modal analysis: minimizing the boundary effect and effectively simulating the shear deformation. The following boundary conditions were implemented: (1) lateral excitation was defined at the base along the longitudinal direction; (2) at any given height, the degrees of freedom along the left and right boundaries were tied together (both longitudinally and vertically using the penalty method); and (3) the ground surface was assumed to be flat and free of loadings. To ensure computational accuracy and to reduce the computation time, quadrilateral elements (CPE4R for soil and CPE4 for structure) were adopted. The element sizes were 0.03 m for the model soil and 0.01 m for the model structure. The first and second order modes of the three-arch type model structure are shown in Fig. 31. It is clear that the deformation of the three-arch type structure was mainly influenced by the first-order mode experiencing horizontal motion.

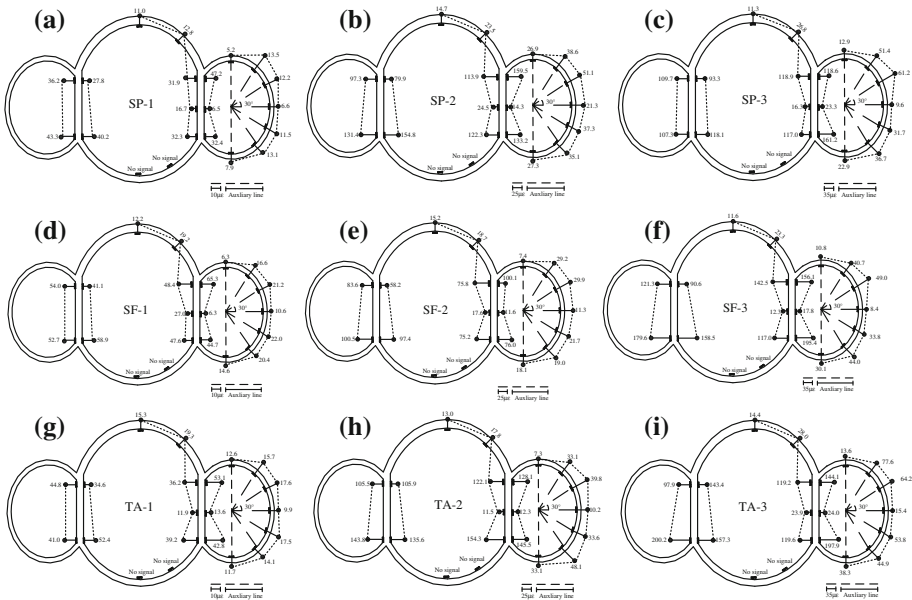


Fig. 30 Peak tensile strains of the model structure for different input motions (unit: $\mu\epsilon$)

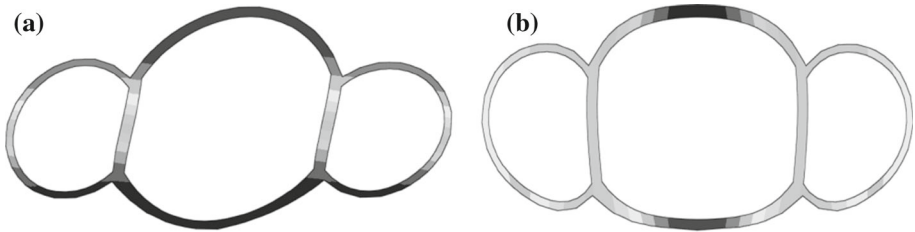


Fig. 31 The first and second modal shape of the model structure. **a** First modal shape. **b** Second modal shape

Based on the speculative tensile yield strength of the micro-concrete, the ultimate tensile strain of the micro-concrete was approximately $95 \mu\epsilon$. A variety of the natural frequencies can be used to characterize the variations in stiffness and damage of the model structure. The relationship between the maximum peak tensile strain and the natural frequency of the model structure is shown in Fig. 32. It is clear that the maximum value of the peak tensile strain located at the top of the right pillar (point S1–12) induced by the Shifang ground motion for the test cases with $\text{PGA} = 0.1 \text{ g}$ is $65.3 \mu\epsilon$. This value was far smaller than the ultimate tensile strain of $95 \mu\epsilon$ of the micro-concrete. The natural frequency of 9.62 Hz of the model structure tested by the first flat noise test did not decrease. However, the peak tensile strain located at the top and bottom of the pillars was considerably larger than the ultimate tensile strain of $95 \mu\epsilon$ of the micro-concrete for the test cases with $\text{PGA} = 0.3$ and 0.5 g . The natural frequency of the structural model decreased from 9.62 to 8.97 Hz and 8.06 Hz for $\text{PGA} = 0.3$ and 0.5 g , respectively.

The peak tensile strain distribution at the primary and secondary observation sections are shown in Fig. 33. The tensile strain at the primary and secondary sections varied significantly, which exhibited remarkable spatial effects. This may be caused by different liquefaction

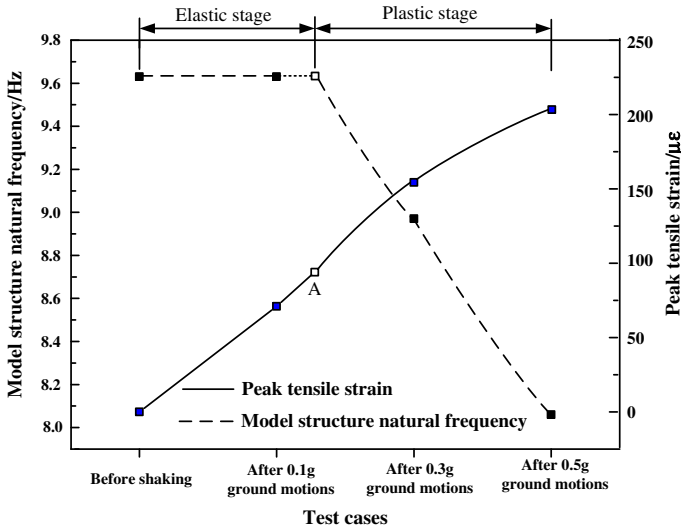


Fig. 32 The relationship between the natural frequency and maximum value of the peak tensile strain of the model structure

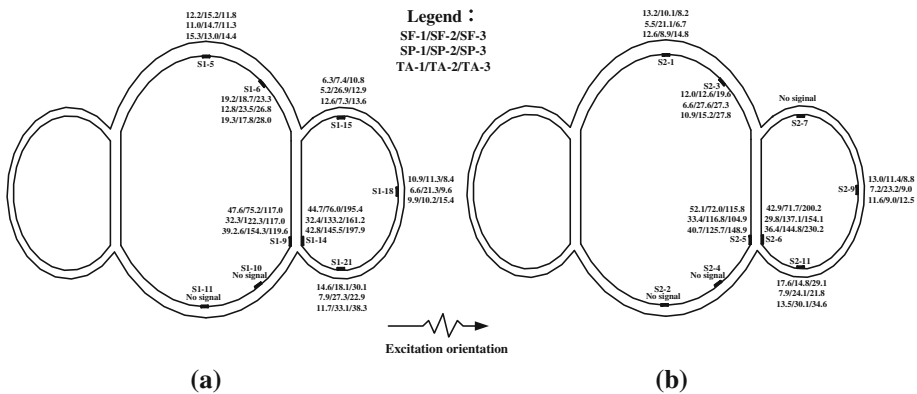


Fig. 33 Distribution of the peak tensile strain at different cross-sections of the model structure (unit: $\mu\epsilon$). **a** Primary observation plan. **b** Secondary observation plan

potentials of the soil surrounding the model structure. The quantitative differences of the soil liquefaction potential in the transverse direction are shown in Sect. 4.1.3. Figure 34a shows the macroscopic phenomenon of the ground surface after tests, from which the difference in soil liquefaction along the structure longitudinal direction can be observed. Soil liquefaction in region A and region B near the model box inner membrane was significantly more serious than the region where the model structure was installed. Figure 34b shows a schematic diagram of the additional forces acting on the model structure induced by the liquefiable soil with different liquefaction potential in different regions of the model box. The asymmetry of the additional forces causes the difference in the stress distribution at different cross sections of the model structure. Because the three-arch type model structure had a large longitudinal stiffness, an uneven stress distribution in the model structure was not significant in the test cases. However, for segment joints of the tunnel structures in practical engineering whose longitu-

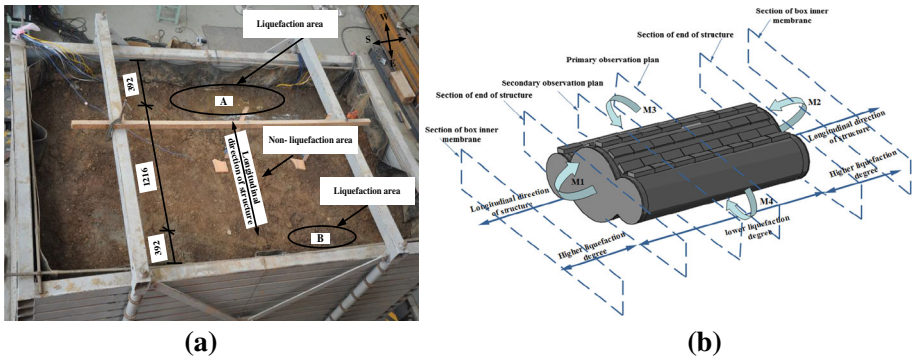


Fig. 34 The schematic diagram of the additional stress on the model structure because soil liquefaction (unit: mm). **a** Macroscopic phenomenon on the ground surface and **b** a schematic diagram of the additional stress on the model structure

dinal flexibility is larger than the model structure in this test, the adverse effects of the uneven distribution of the longitudinal stress induced by the soil liquefaction should not be ignored.

5 Concluding remarks

A series of shaking table tests were conducted to investigate the damage mechanisms of a three-arch type subway station structure in liquefiable soil under strong motions. Particular attention is focused on new measuring methods: the vision-based displacement test and the fiber Bragg grating test to measure the strain response of the galvanized steel wire. The main results are as follows:

- (1) The buildup of excess pore pressure of the model soil mainly proceeded through two increasing stages. Initially, the excess pore pressure increased very slowly. Then, a dramatic increase in the peak excess pore pressure ratio coincided with a dramatic increase in the Arias intensity. The peak acceleration of the model soil also almost coincided with the moment that the excess pore pressure ratio of the model soil equaled approximately 1. The lowest liquefaction potential regions were located in the region beneath the model structure for test cases with $PGA = 0.1\text{ g}$ and the bottom region of the ground for test cases with $PGA = 0.3$ and 0.5 g .
- (2) The dominant frequency of the input motions with lower and higher PGA has an inverse effect on the soil acceleration amplification effect. When the PGA of input motions increased, the soil softened and the phenomenon of high frequency filtering and low frequency amplification effect of the liquefied soil were more obvious.
- (3) Similar to the results of the seismic behavior of underground structures in the existing literature, the maximum tension strain of the three-arch type subway structure was located at the top and bottom of the center pillars, which means that the pillars were too weak to resist the soil lateral deformations induced by strong earthquakes. The peak tensile strains at the primary and secondary observation sections were quite different, exhibiting remarkable spatial effects. The deformation of the three-arch type structure was mainly influenced by the first-order mode under horizontal motions where the peak tensile strain increased and the natural frequency of model structure decreased. The phenomenon of the model structure moving upward with respect to the model soil occurred under strong motions.

Acknowledgments The authors gratefully acknowledge the financial support of this study by the Major Research Plan Integration Project of the Natural Science Foundation of China (No. 91215301) and the Project of Construction of Innovative Teams and Teacher Career Development for Universities and Colleges in the Beijing Municipality (No. IDHT20130512). Special thanks to the staff at Jiangsu Province Key Laboratory of Civil Engineering and Disaster Prevention and Mitigation, attached to the Nanjing University of Technology, and in particular to Mr. Xiaojian Han.

References

- An X, Shaww AA, Maekawa K (1997) The collapse mechanism of subway station during the Great Hanshin earthquake. *Cem Concr Compos* 19:241–257
- Arias A (1970) A measure of earthquake intensity. In: Hansen RJ (ed) *Seismic design for nuclear power plants*. MIT Press, Cambridge
- Bennett MJ, McLaughlin PV, Sarmiento JS, Youd TL (1984) Geotechnical investigation of liquefaction sites. Imperial Valley, California. US Geological Survey, Open-File Report 84–252, 103 pp
- Chen S, Chen G (2013) Vision-based dynamic displacement test software (version: 1.0). Software copyright in China. 2013SR022133. 2013-03-11
- Chen GX, Zhang HY, Du XL et al (2007) Analysis of large-scale shaking table test of dynamic soil–subway station interaction. *Earthq Eng Vib* 27(2):171–176 (in Chinese)
- Chen G, Zuo X, Wang Z et al (2010a) Shaking table model test of subway station structure at liquefiable ground under far field and near field ground motion. *J Zhejiang Univ Eng Sci* 44(10):1955–1961 (in Chinese)
- Chen G, Zuo X, Wang Z et al (2010b) Large scale shaking table test study of the dynamic damage behavior of subway station structure in liquefiable foundation under near-fault and far-field ground motions. *China Civ Eng J* 43(12):120–126 (in Chinese)
- Chen G, Wang Z, Zuo X et al (2010c) Development of laminar shear soil container for shaking table tests. *Chin J Geotech Eng* 32(1):89–97 (in Chinese)
- Chen G, Wang B, Sun T (2012) Dynamic shear modulus of saturated Nanjing fine sand in large scale shaking table tests. *Chin J Geotech Eng* 34(4):582–590 (in Chinese)
- Chen G, Wang Z, Zuo X et al (2013) Shaking table test on the seismic failure characteristics of a subway station structure on liquefiable ground. *Earthq Eng Struct Dyn* 42:1489–1507
- Han C (2011) Study on the response and design method of circular tunnel under severe earthquakes. Zhejiang University, Hangzhou (in Chinese)
- Han X, Zuo X, Chen G (2010) 98 channels' dynamic signal acquisition system development for shaking table test based on virtual instrument technology. *J Disaster Prev Mitg Eng* 30(5):503–508 (in Chinese)
- Hashash Y, Hook J, Schmidt B, Yao J (2001) Seismic design and analysis of underground structures. *Tunneling and Underground Space Technology* 16:247–293
- Holzer TL, Youd TL (2007) Liquefaction, ground oscillation, and soil deformation at the Wildlife Array, California. *Bull Seismol Soc Am* 97(3):961–976
- Hyndmana RJ, Koehlerb AB (2006) Another look at measures of forecast accuracy. *Int J Forecast* 22:679
- Iwatate T, Kobayashi Y, Kusu H et al (2000) Investigation and shaking table tests of subway structures of the Hyogoken-Nambu earthquake. In: *Proceedings of the 12WCEE*
- Kammerer AM, Wu J, Riemer MF, Pestana JM, Seed RB (2001) Use of cyclic simple shear testing in evaluation of the deformation potential of liquefiable soils. In: 4th international conference on recent advances in geotechnical earthquake engineering, San Diego
- Kattis SE, Beskos DE, Cheng AD (2003) 2D dynamic response of unlined and lined tunnels in poroelastic soil to harmonic body waves. *Earthq Eng Struct Dyn* 32(1):97–110
- Koga Y, Matsuo O (1990) Shaking table tests of embankments resting on liquefaction sandy ground. *Soils Found* 30(4):162–174
- Ling G, Shipai L, Juan N (2009) Damages of metro structures due to earthquake and corresponding treatment measures. *Mod Tunnel Technol* 46(4):36–41 (in Chinese)
- Ling D-S, Guo H, Cai WJ et al (2012) Research on seismic damage of metro station with centrifuge shaking table model test. *J Zhejiang Univ Eng Sci* 10:1955–1961 (in Chinese)
- Liu J, Liu X, Wang Z et al (2010) Dynamic centrifuge model test of a soil–structure interaction system. *Chin J Civ Eng* 43(11):114–121 (in Chinese)
- Maymand PJ (1998) Shaking table scale model tests of nonlinear soil–pile–superstructure interaction in soft clay. University of California, Berkeley

- Ohtomo K, Suehiro T, Kawai T et al (2001) Research on streamlining seismic safety evaluation of underground reinforced concrete duct-type structures in nuclear power stations—Part-2. Experimental aspects of laminar shear sand box excitation tests with embedded RC models. Transactions, SMiRT 16, Washington, DC, August 2001, Paper no. 1298
- Ohtomo K, Suehiro T, Kawai T et al (2003) Substantial cross section plastic deformation of underground reinforced concrete structures during strong earthquakes. In: Proceedings of Japan Society of Civil Engineering, no. 724/I-62, pp 157–175 (in Japanese)
- Samata S, Ohuch H, Matsuda T (1997) A study of the damage of subway structures during the 1995 Hanshin-Awaji earthquake. Cem Concr Compos 19:223–239
- Schiff AJ (ed) (1998) Hyogoken-Nanbu (Kobe) earthquake of January 17, 1995 lifeline performance. Technical Council on Lifeline Earthquake Engineering Monograph, no. 14. ASCE
- Sedarat H, Kozak A, Hashash YMA (2009) Contact interface in seismic analysis of circular tunnels. Tunn Undergr Space Technol 24:482–490
- Seed HB, Lee KL (1966) Liquefaction of saturated sands during cyclic loading. J Soil Mech Found Eng ASCE 92:105–134
- Tamari Y, Towhata I (2003) Seismic soil–structure interaction of cross sections of flexible underground structures subjected to soil liquefaction. Soil Found 43(2):69–87
- Yasuda S, Harada K, Ishikawa K et al (2012) Characteristics of liquefaction in Tokyo Bay area by the 2011 Great East Japan earthquake. Soils Found 52(5):793–810